Instructions for use

ARTICLE

Co$_x$Ni$_{1-x}$O-NiCo$_2$O$_4$/rGO Synergistic Bifunctional Electrocatalysts for High-Rate Rechargeable Zinc-Air Battery

Zixuan Huang,[a] Mai Thanh Nguyen,[*a] Wei Jian Sim,[a] Masayuki Takahashi,[a] Soorathep Kheawhom[b] and Tetsu Yonezawa[*a]

Bifunctional catalysts containing spinel NiCo$_2$O$_4$ and Co$_x$Ni$_{1-x}$O bimetallic oxide nanoparticles embedded on reduced graphene oxides (rGO), CoNi/rGO, were obtained by thermal decomposition of metal nitrates and graphene oxides (GO). For the first time, we report the correlation of the catalytic activities in oxygen reduction reaction (ORR) and oxygen evolution reaction (OER) at low current density (< 30 mA·cm^{-2}) and zinc-air battery (ZAB) performance at high current density of 100 mA·cm^{-2} with the structures of CoNi/rGO catalysts of different Co:Ni molar ratio and metal loading. A layer of 2-3 nm NiCo$_2$O$_4$ and Co-rich Co$_x$Ni$_{1-x}$O nanoparticles on rGO exhibited synergistic ORR catalytic effect. In contrast, NiO and big sized Ni-rich Co$_x$Ni$_{1-x}$O nanoparticles (10-20 nm) exhibited poor ORR and OER performance at low current density. No synergetic effect of Co and Ni oxides were found in OER at low current density of electrochemical test. The battery test at high current density revealed the best cycle stability of CoNi/rGO-5/5 with equimolar of Co and Ni and medium metal loading. This is owing to the synergetic OER performance with the lowest charge voltage at high current density and the best ORR activity with the highest electron transfer numbers of 3.63. This is related to the highest Co:Ni ratio of the small sized Co$_x$Ni$_{1-x}$O bimetallic oxide and high amount of spinel NiCo$_2$O$_4$ nanoparticles. Corrosion during charging was found to be the limiting factor of the long-term cycle stability at high current density.

1. Introduction

"Affordable, reliable, sustainable, and modern energy" for all is the 7th of 17 sustainable development goals (SDGs) in the urgent call from the United Nation for action by all countries.[1] With the growing demand of energy, depletion of fossil fuels, and heading towards net zero emission, the development of green rechargeable batteries, which can couple with fast conversion and storage of renewable energy resources, has been demanded.[2] For that purpose, rechargeable aqueous zinc-air batteries (ZABs) with high theoretical energy density of 1086 W·h·kg^{-1}, environmental friendliness, abundant materials resource, low cost, and safety have attracted much attention.[3-6] ZABs present a great prospect as an energy storage device on a large scale.[4]

A typical ZAB contains negative electrode (Zn anode), electrolyte, and positive electrode which is the air cathode with catalyst, current collector, and gas diffusion layer (GDL). On the air cathode of rechargeable ZAB, oxygen reduction reaction (ORR) and oxygen evolution reaction (OER) occurs when discharging and charging, respectively.[7-9] Because of the sluggish reaction kinetics of both ORR and OER, they are the rate determining steps of the whole electrochemical reaction in ZABs. Besides, high overpotential of OER (over 2.0 V vs. RHE) can cause corrosion of the cathode.[10] Hence, bifunctional electrocatalyst with high catalytic activities and stability is needed.[11,12]

Recently, electrocatalysts based on non-precious and earth-abundant transition metal oxides of low cost have been studied for replacing the high-cost and scarce conventional Pt and IrO$_2$ catalysts.[12-17] Moreover, some studies suggested that bimetallic oxide catalysts, such as binary oxides of Co, Fe, and Ni, performed better than monometallic oxides in ORR and OER.[18-22] For example, NiO$_x$-based compounds are promising ORR/OER catalysts in alkaline media and Co-doped NiO$_x$ catalysts exhibit synergistic effect.[20] Cui prepared a core-ring hexagonal structure Co-rich spinel NiCo$_2$O$_4$, which exhibited an OER overpotential of 0.315 V (vs. SCE) in alkaline electrolyte at a current density of 100 mA·cm^{-2}, better than Co$_3$O$_4$.[21] Prabu reported a one-dimensional NiCo$_2$O$_4$ catalyst by using electrospinning, which showed an electrocatalytic activity with

a. Division of Materials Science and Engineering, Faculty of Engineering, Hokkaido University, Kita 13 Nishi 8, Kita-ku, Sapporo, Hokkaido 060-8628, Japan
b. Department of Chemical Engineering, Faculty of Engineering, Chulalongkorn University, Phayathai Road Pathumwan, Bangkok 10330, Thailand
*Tetsu Yonezawa, Email: tetsu@eng.hokudai.ac.jp
*Mai Thanh Nguyen, Email: mai_nt@eng.hokudai.ac.jp

ORR onset potential of 0.93 V and OER potential of 1.62 V at 10 mA·cm^{-2} (vs. RHE), better than the noble metal catalyst.[22] However, so far, the stability and performance evaluation of binary oxide catalysts in charging and discharging of ZABs have been carried out at relatively low current density (≤ 30 mA·cm^{-2})[23-25] and typically in short charge/discharge time (< 60 min).[26-34] Furthermore, recently we found that the gap between bifunctional catalytic performance from electrochemical test (polarization) and battery performance at low current densities does not allow for a direct judgment and prediction of the ZAB performance in terms of capacity and cycle stability at higher current densities from the existing literature.[35] Moreover, our finding indicates that the loading of mixed CoFe$_2$O$_4$ and CoO on rGO as catalysts for ZAB evaluated at current density of 100 mA·cm^{-2} for 60 min charge and 60 min discharge per cycle impact the battery performance. In new direction of ZAB operating at such extreme conditions, not only the stability of the battery but also understanding the role of each catalyst components and their contributions to the battery performance are demanded.[35]

In this work, we aimed at evaluating ZAB performance at high current density of 100 mA·cm^{-2} in each 60 min charge and 60 min discharge per cycle, which are severe conditions, for the first time. Such a high current density can allow for high-rate charge/discharge which enables high efficient energy storage/conversion for harvesting renewable energies in large-scale or for grid applications. However, poor electron conductivity hinders the catalytic activity of bimetallic oxides in electrochemical reactions. Graphene oxides (GO), derived from graphite, with structural defects and various types of oxygen functional groups can provides large specific surface area to improve the dispersion and electron tunnels of metal oxides. After reduction, reduced GO (rGO) is a good electrically conductive substrate with high electron conductivity. A series of bifunctional ORR/OER electrocatalysts for ZAB was prepared using a single-step thermal decomposition of Co and Ni nitrate and graphene oxide (GO). The formed hybrid materials, binary CoNi oxide on reduced GO (rGO), are called CoNi/rGO. We chose to synthesize CoNi/rGO to take advantages of electron conductive rGO sheets, their capability of dispersing the nonconductive CoNi oxide, and the synergetic effect of forming binary CoNi oxides.[19,36]

In our work, the molar ratio of Co:Ni and CoNi loading amount on GO were varied. The formed catalysts were examined for their morphological and crystal structures, electrochemical catalytic properties in ORR and OER, and ZAB discharge-charge cycle performance at the air cathode. Our results elucidated the effect of the composition, crystal structure, size, and dispersion on rGO of the CoNi oxide catalysts on ORR/OER electrochemical catalytic performance, and on long-term discharge-charge battery cycle stability. It was found that large nanoparticles of Ni-rich Co$_x$Ni$_{1-x}$O bimetallic oxides and small nanoparticles of spinel NiCo$_2$O$_4$ and Co-rich Co$_x$Ni$_{1-x}$O bimetallic oxides uniformly anchored on the rGO sheets (CoNi/rGO) wherein spinel is a minor phase. ORR activity was found to correlate with Co-rich Co$_x$Ni$_{1-x}$O bimetallic oxides and spinel NiCo$_2$O$_4$ whereas the OER activity of CoO and Co-rich

oxide was higher than NiO. The binary CoNi oxide on rGO revealed synergetic ORR activity compared to rGO, only Co oxide, and only Ni oxide in electrochemical test. We did not observe the synergetic OER activity at low current density (≤ 20 mA·cm^{-2}). In battery test, however, the synergetic OER activity of binary CoNi/rGO was evident based on the lower charge voltage over cycles and the improved cycle stability. The ZAB cells containing CoNi/rGO catalysts with equimolar ratio of Co to Ni displayed the highest cycling stability of 31 consecutive cycles (1 h charge and 1 h discharge each cycle) at 100 mA·cm^{-2} and the lowest charging potentials over cycles among other CoNi/rGO catalysts. This came from the ideal metal loading, the abundant Co-rich bimetallic oxides (Co:Ni nearly 2:1 mol/mol), and spinel oxides well dispersed on rGO. Our results demonstrated promising application of CoNi/rGO as air cathode catalyst in rechargeable ZABs under high current density.

2. Experimental

2.1 Chemicals and Materials

All chemicals were analytical grade and used without further purification. Graphite powder, potassium hydroxide (KOH, 85 %), sulfuric acid (H$_2$SO$_4$, 98 %), cobalt(II) nitrate hexahydrate (Co(NO$_3$)$_2$·6H$_2$O, 98%), and 5wt% platinum-activated carbon (Pt/C, 5 % Pt) as the reference catalyst were purchased from Wako (Japan). Hydrogen peroxide (H$_2$O$_2$, 35 %), sodium nitrate (NaNO$_3$, 99.0 %), and potassium permanganate (KMnO$_4$, 99.3 %) were purchased from Junsei Chemical Co., Ltd. (Japan). Hydrochloric acid (HCl, 35-37 %), nickel(II) nitrate hexahydrate (Ni(NO$_3$)$_2$·6H$_2$O, 98 %) and zinc chloride (ZnCl$_2$, 98.0 %) were purchased from Kanto Chemical Co., Inc. (Japan). Nafion perfluorinated resin solution (5 %) was purchased from Sigma-Aldrich (USA). Expanded polytetrafluoroethylene (ePTFE, SEF-010(HB)) was purchased from Chukoh Chemical Industries, Ltd. (Japan). Zn plates (>99 %, 3 mm, Standard Test Piece K.K) were used as anodes. Nickel foams (Celmet #8, Sumitomo Electric Industries Ltd., Japan) were used for making air cathode. Sigracet 22 BB purchased from SGL CARBON GmbH (Germany) was used as the GDL. Water was purified using Organo Puric System (> 18 MΩ).

2.2 Synthesis of GO

The synthesis of GO was performed using the modified Hummers' method according to Fu et al.[37] Graphite powder (2.0 g) was mixed with NaNO$_3$ (1.0 g) and concentrated H$_2$SO$_4$ (100 mL) for 30 min at 0 °C, and then KMnO$_4$ (8.0 g) was added to the mixture and stirred for 3 h at 35 °C. 200 mL of pure water was then added to the mixture and maintained at 98 °C for 1 h. The resulting mixture was washed by H$_2$O$_2$, HCl, and DI water subsequently to obtain a neutral pH. Then the mixture was dried in vacuum at 60 °C for 24 h and GO was obtained.

2.3 Synthesis of CoNi/rGO catalyst

Figure 1 illustrates the synthesis of CoNi/rGO and the quantities of the materials used are tabulated in **Table 1**.
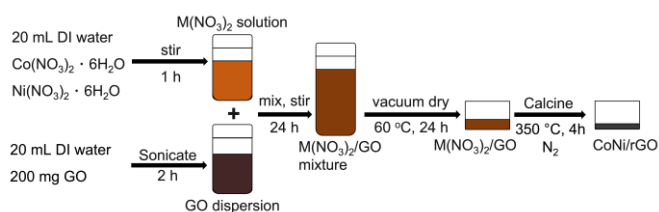
Figure 1. Schematic illustration of the synthesis of CoNi/rGO catalysts.

Initially, 200 mg of GO was added into 20 mL pure water and sonicated for 2 h to obtain the GO dispersion. $Co(NO_3)_2 \cdot 6H_2O$ and $Ni(NO_3)_2 \cdot 6H_2O$ were added in to 20 mL of pure water and stirred for 1 h to obtain metal nitrate ($M(NO_3)_2$) solution. Then the solution of metal nitrates was added into GO dispersion under vigorous stirring. The resulting mixture was then stirred for 24 h to obtain a homogeneous mixture and subsequently dried in a vacuum oven at 60 °C. After that, the dried sample was put into a tube furnace and kept at room temperature (RT) for 30 min under N_2 flow. Then it was calcined under N_2 flow (0.5 L·min^{-1}). The heating speeds were 5 °C·min^{-1} from RT to 120 °C, 0.5 °C·min^{-1} from 120 to 200 °C, and 5 °C·min^{-1} from 200 to 350 °C. The sample was kept under 350 °C for 4 h to obtain CoNi/rGO before it was cooled down to RT naturally. The temperature profile of the synthesis was recorded (**Figure S1**).

2.4 Materials Characterization

The crystal structure of the as-prepared samples was investigated by X-ray diffraction (XRD) conducted on a Rigaku

MiniFlex II Desktop X-ray diffractometer with Cu-Kα radiation at scanning speed of 5 °·min^{-1}. The material morphology was observed using a scanning electron microscope (SEM, JEOL JSM-6701F, 15 kV) and a transmission electron microscope (TEM, JEOL JEM-2000FX, 200 kV). Selected area electron diffraction (SAED) patterns of the samples were collected using TEM. A spherical aberration corrected scanning TEM (STEM, JEOL JEM-ARM200F, 200 kV) equipped with energy dispersive X-ray spectrometer (EDS) was used for the analysis of the fine structure and elemental composition of the samples. High-annular dark field (HAADF) images of the samples were obtained using STEM. Thermogravimetric analysis and differential thermal analysis (TGA-DTA) of the metal nitrates in GO were conducted using CoNi/rGO-10/0, 5/5 and 0/10 under N_2 gas at flow rate of 100 mL·min^{-1} from RT to 350 °C.

2.5 Electrochemical Test

Electrochemical tests were carried out using HZ-Pro S4 (Hokuto Denko, Japan) multi electrochemical measurement system at 25 °C. A conventional three-electrode system was employed to investigate the electrocatalytic performance of the as-prepared catalysts. The working electrode was a rotating disk electrode (RDE) with a glassy carbon (GC) disk (electrode area: 0.1962 cm^2). The loading amount of the catalyst was 0.5 mg·cm^{-2}. The catalyst ink was prepared by dispersing 5 mg of the as-prepared catalysts into 1 mL of 0.5 wt% Nafion-IPA solution. Then catalyst ink (20 μL) was dropcasted onto the glassy-carbon disk of the RDE. 1 M KOH aqueous solution was used as the electrolyte.

Table 1. Quantities of materials used in all CoNi/rGO catalysts.

Samples	m_{Co} (mg)	m_{Ni} (mg)	$Co(NO_3)_2 \cdot 6H_2O$ (mmol)	$Ni(NO_3)_2 \cdot 6H_2O$ (mmol)	Co:Ni (mol/mol)	m_{GO} (mg)	CoNi wt%[d]
CoNi/rGO-i/j[a]							
10/0	200.00	0.00	3.39	0.00	10:0		
8/2	160.13	39.87	2.72	0.68	8:2		
6/4	120.20	79.80	2.04	1.36	6:4		
5/5[c]	100.20	99.80	1.70	1.70	5:5	200	50
4/6	80.20	119.80	1.36	2.04	4:6		
2/8	40.13	159.87	0.68	2.72	2:8		
0/10	0.00	200.00	0.00	3.41	0:10		
CoNi/rGO-w wt%[b]							
0 wt%	-	200	0				
20 wt%	25.0	25.0	0.43	0.43			20
40 wt%	66.7	66.7	1.13	1.13			40
50 wt%[c]	100.0	100.0	1.70	1.70	5:5		50
60 wt%	150.0	150.0	2.55	2.55			60
80 wt%	400.0	400.0	6.80	6.80			80
100 wt%	100.0	100.0	1.70	1.70		0	100

[a]Samples of CoNi oxide with molar ratio varied in rGO were labeled as CoNi/rGO-i/j with Co:Ni = i:j (mol/mol); [b]samples with different metal loadings were labeled as CoNi/rGO-w wt% where "w" is the metal loading; [c]CoNi/rGO-5/5 and CoNi/rGO-50% are the same sample; [d]$CoNi\ wt\% = \frac{m_{Co}+m_{Ni}}{m_{GO}+m_{Co}+m_{Ni}}$ $(Eq.\ 1)$

Hg/HgO and Pt wire were used as the reference electrode and the counter electrode, respectively. Before electrochemical tests for ORR, the electrolyte was purged with Ar (Ar bubbling) for 30 min and then the electrode was electrochemically cleaned for 30 cycles between 0.4 and 1.1 V (vs RHE) at scan rate of 50 mV·s^{-1}. The electrolyte was then bubbled with O_2 for 30 min to achieve O_2-saturated electrolyte solution. After electrode cleaning, cyclic voltammetry (CV) was carried out in both Ar-saturated and O_2-saturated electrolytes at a scan speed of 50 mV·s^{-1}. Linear sweep voltammetry (LSV) was conducted in O_2-saturated electrolyte at various rotation speeds of 400, 900, 1225, 1600, 2025 and 2500 rpm of the RDE at a scan rate of 5 mV·s^{-1}. Using the same electrochemically cleaned electrode from ORR tests, OER test was carried out by LSV in Ar-saturated electrolyte at a rotation speed of 1600 rpm and a scan rate of 5 mV·s^{-1} from 0.8 to 1.9 V (vs RHE).

2.6 ZAB Test

The rechargeable ZABs were prepared using lab-scale acrylic electrochemical cells (**Figure S2**). A solution of 6 M KOH mixed with 0.2 M $ZnCl_2$ was used as the electrolyte. Zn plates (3.5 cm × 5 cm × 0.3 cm) were used as the anodes. The air cathode was composed of a Ni foam with catalyst, gas diffusion layer, and an ePTFE film. The catalyst ink was prepared by dispersing 1 mg of as-prepared catalysts into 100 μL of 0.5 wt% Nafion-IPA solution and sonicated for 30 min. Then the ink was dripped slowly onto the Ni foam and dried. The area of the cathode in contact with the electrolyte was 1 cm^2. The loading of the catalyst on the cathode was 1 mg·cm^{-2}. Discharge-charge cycle performance of ZABs was tested by using a Neware BTS4000 series battery testing system. The current density was set at 100 mA·cm^{-2} with 1 h discharging and 1 h charging for each cycle.

3. Results and Discussion
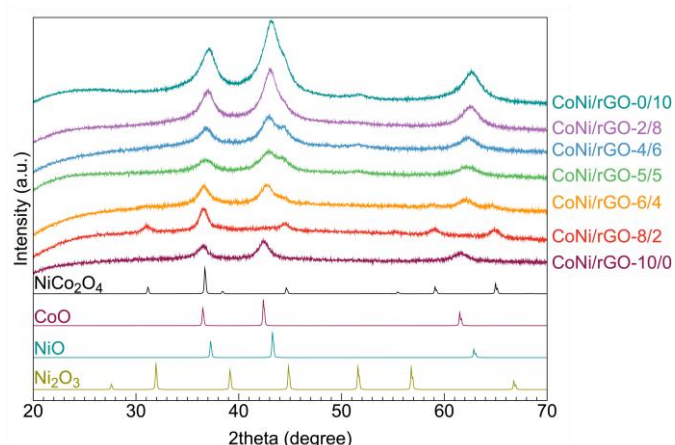
3.1 Structure of the CoNi/rGO Catalysts

Figure 2. XRD patterns of the CoNi/rGO-i/j samples of 50 wt% metal loading and different Co:Ni molar ratios (from the top pattern to the 7th pattern downwards) of 0/10 (cyan), 2/8 (violet), 4/6 (blue), 5/5 (green), 6/4 (orange), 8/2 (red), and 10/0 (purple). The standard patterns of $NiCo_2O_4$ (JCPDS No. 00-020-0781, black), CoO (JCPDS No. 00-048-1719, violet), NiO (JCPDS No. 00-047-1049, cyan) and Ni_2O_3 (JCPDS No. 00-014-0481, green) are shown at the bottom of the graph.

XRD was used to determine the crystalline structure and to estimate the mass ratio of different phases present in the as-prepared catalysts. As shown in **Figure 2**, CoNi/rGO-10/0 (only Co oxide sample) showed only characteristic peaks corresponding to CoO. In CoNi/rGO-0/10 sample (only Ni oxide sample), the peak at 43.3 ° in 2ϑ corresponded to NiO as the major phase. Small peaks located at 44.8 and 51.6 ° in 2θ corresponded to the (200) and (112) planes, respectively, of Ni_2O_3 as the minor phase. In Co rich sample, i.e., CoNi/rGO-8/2, XRD peaks matched well with spinel $NiCo_2O_4$; the characteristic peaks of $NiCo_2O_4$, which are not overlap with the XRD peaks of other mono-oxides, at 31.2, 59, and 65 ° in 2θ were observed. In spinel $NiCo_2O_4$, Ni and Co occupy tetragonal and octahedral sites, respectively; the two octahedral sites share an edge while octahedral and tetragonal sites share a vertex. In the precursors, the feeding ratio of Co:Ni = 8:2 (mol/mol) is higher than the stoichiometric ratio of Co:Ni = 2:1 (mol/mol) in stoichiometric $NiCo_2O_4$. Thus, the resulting CoNi/rGO-8/2 catalyst can contain non-stoichiometric spinel structure (Co rich) wherein some Co can also occupy tetragonal site of the spinel lattice. Moreover, different from monometallic oxide catalysts wherein CoNi/rGO-10/0 matched with CoO and CoNi/rGO-0/10 contained mainly NiO and the minor Ni_2O_3 phase, a part of Co atoms in spinel structure of CoNi/rGO-8/2 exists as Co(III) (Co_2O_3) while Ni atoms have a valence of 2 (NiO). As Ni molar ratio further increased, i.e., for sample CoNi/rGO-6/4, the XRD peaks belonging to spinel $NiCo_2O_4$ decreased; only the peak at 44.6 ° in 2θ for the (400) plane of spinel $NiCo_2O_4$ remained visible without overlapping with other monometallic oxides.

Meanwhile, the XRD peaks belonging to CoO and NiO in the form of bimetallic oxide, $Co_xNi_{1-x}O$ where $0\leqslant x\leqslant1$, increased and $Co_xNi_{1-x}O$ became the main phase. The positions of three main diffraction peaks of CoNi/rGO-6/4 at about 37.2, 43.2, and 63.0 ° in 2θ were in between the reference peaks of CoO and NiO corresponding to the (111), (200), and (220) planes. This suggests that Co and Ni are in randomly mixed state in the $Co_xNi_{1-x}O$ bimetallic oxide lattice. When Ni ratio increased, that is, Co:Ni (mol/mol) ratio decreased from 6:4 (Co rich) to 2:8 (Ni rich), $Co_xNi_{1-x}O$ bimetallic oxides were still the major phase and their peaks shifted from that of CoO to NiO. This result further indicates that the metal oxides existed in a form of $Co_xNi_{1-x}O$ bimetallic oxides instead of a physical mixture of CoO and NiO. Vegard's law[38, 39] was used to calculate the "x" value in $Co_xNi_{1-x}O$ bimetallic oxides (**Table 2**) for CoNi/rGO-6/4, 5/5, 4/6, and 2/8 samples (details in SI) based on the (200) peak position of the samples between that of CoO (42.388 °) and NiO (43.280 °). The results (**Table 2**) indicate that in CoNi/rGO-6/4, 5/5, 4/6, and 2/8, the Co:Ni ratios in $Co_xNi_{1-x}O$ bimetallic oxides are slightly lower than the feeding ratios (5-15 % lower). Thus, a part of Co atoms that did not incorporate in the bimetallic oxides, exist in spinel $NiCo_2O_4$. Because the molar ratios of Co:Ni in $Co_xNi_{1-x}O$ were of 5-15 % lower than that in the feeding ratios and the $Co_xNi_{1-x}O$ presented as the main phase in the XRD patterns of samples CoNi/rGO-6/4, 5/5, 4/6, and 2/8, it is expected that the minor spinel $NiCo_2O_4$ phase existed in stoichiometric form.

Table 2. The amount of different phases of metal oxides calculated from XRD

Samples CoNi/rGO-i/j	Feeding ratio		$2\theta_{(200)}$ of $Co_xNi_{1-x}O$ (°)	"x" in $Co_xNi_{1-x}O$[a]	% Co deficiency[b]	Calculated molar ratios		
	Co	Ni				$Co_xNi_{1-x}O$	$NiCo_2O_4$	$NiCo_2O_4$ mol. %
10/0	10	0	42.380	1	1	1[c]	0	0
8/2	8	2	NA	NA	NA	0	1[d]	100[d]
6/4	6	4	42.785	0.57	5	6.896	1.034	13
5/5	5	5	42.905	0.43	14	7.042	0.986	12
4/6	4	6	42.965	0.37	8	8.989	0.337	4
2/8	2	8	43.136	0.17	15	9.396	0.201	2
0/10	0	10	43.265	~0	~0	1[e]	0	0

[a]calculated from (200) peak position of $Co_xNi_{1-x}O$ based on Vegard law; [b]deficient Co (in %) in $Co_xNi_{1-x}O$ compared with in the feeding ratio; [c]only CoO; [d]Co-rich nonstoichiometric spinel $NiCo_2O_4$; [e]mostly NiO with minor Ni_2O_3; NA: not applicable

Using this assumption and based on the obtained "x" value of $Co_xNi_{1-x}O$ and the feeding ratio of Co and Ni, the molar ratios of $Co_xNi_{1-x}O$ bimetallic oxide and the stoichiometric spinel $NiCo_2O_4$ phases were estimated (see SI for details) and shown in **Table 2**. The molar percentages of spinel $NiCo_2O_4$ (**Table 2**) in Co-rich samples CoNi/rGO-6/4 and 5/5 are of 13 and 12 %, respectively, which are higher than that in Ni-rich samples: CoNi/rGO-4/6 (4%) and CoNi/rGO-2/8 (2%). Note that 100 % spinel $NiCo_2O_4$ in Co-rich sample (CoNi/rGO-4/6) written in **Table 2** refers to Co-rich nonstoichiometric spinel $NiCo_2O_4$ whereas zero % spinel is for samples of monometallic oxides according to XRD results.

XRD results of samples with equimolar metal ratio and different metal loadings were shown in **Figure S3**. At low metal loadings of 40 wt% or less (samples CoNi/rGO-0, 20, and 40 wt%), a feature broad XRD peak around 25° from the (002) plane of the graphitic carbon was observed.[40] Meanwhile, XRD peaks from metal oxides were not observed due to high content of rGO and low metal loadings. The crystal structures of these samples were analyzed with TEM-SAED (**Figure S4**), which revealed the presence of $Co_xNi_{1-x}O$ and spinel $NiCo_2O_4$. At high metal loadings, CoNi/rGO-50, 60, and 80 wt% displayed the characteristic XRD peaks belonging to $Co_xNi_{1-x}O$ bimetallic oxides and spinel $NiCo_2O_4$. As metal loading increased, the XRD peaks intensity of both $Co_xNi_{1-x}O$ and $NiCo_2O_4$ became stronger relatively to that of the broad peak corresponding to rGO. The relative ratios of spinel $NiCo_2O_4$ and $Co_xNi_{1-x}O$ changed with the metal loading from 50 to 80 wt%, that is, the highest ratio was observed for CoNi/rGO-60 wt% and the lowest one was for CoNi/rGO-80 wt% based on XRD peak intensity of (400) $NiCo_2O_4$ (42-43°) and (200) $Co_xNi_{1-x}O$ (44-45°). Without using GO in calcination, XRD peaks of CoNi/rGO-100 wt% (only metal oxides) matched well with the standard patterns of $NiCo_2O_4$ (major phase) and NiO (minor phase). This suggests an important role of rGO in supporting the formation of $Co_xNi_{1-x}O$ bimetallic oxide as major phase.

The morphology, size, and composition distribution of the catalyst samples were investigated using SEM, TEM, and EDS. **Figure 3a** shows the SEM image and SEM-EDS mapping results of sample CoNi/rGO-5/5, wherein O, Co, and Ni dispersed uniformly on the rGO sheets. Large nanoparticles with the average size of 13.9 ± 3.1 nm on rGO sheets were observed in TEM (**Figure 3b**). The particle size and size distribution did not vary significantly when varying the Co:Ni metal ratio, that is, 14.9 ± 2.6, 18.1 ± 3.4, 15.3 ± 2.9, and 17.9 ± 3.5 nm for samples CoNi/rGO-2/8, 4/6, 6/4, and 8/2, respectively (**Figure S5**). Small oxide nanoparticles on rGO could be present but were not resolved with normal TEM due to the limitation of the machine resolution and little difference in the contrast between rGO and small oxide nanoparticles. The SAED pattern of CoNi/rGO-5/5 (**Figure 3c**) displayed diffraction rings from the (111) plane of $NiCo_2O_4$ and (200) plane from $Co_xNi_{1-x}O$. This result agreed well with the XRD result. SAED patterns of catalysts of other metal ratios are shown in **Figure S5**. Separated large nanoparticles could not be observed in the TEM images of CoNi/rGO-10/0 and 0/10, which were the monometallic oxide catalysts. Particles in these two samples were small and dispersed uniformly on the rGO sheets. Thus, only when both Co and Ni existed in the catalysts, the large nanoparticles were formed.

Varying the metal loading (0-100 wt%) in GO did not affect the particle sizes (10-16 nm on average) but it showed a clear impact on the particle number density and aggregation state (**Figure S4**). For the CoNi/rGO-100%, the sample without rGO, the metal oxides particles aggregated together. The number of large nanoparticles (10-20 nm) and particle accumulation at the edge of the rGO sheets decreased as the metal loading amount decreased. This reveals the role of rGO sheets as the matrix in dispersing metal oxide nanoparticles.
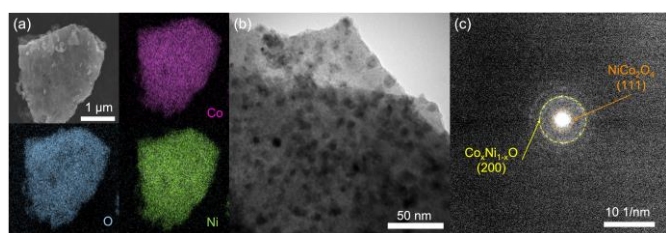
Figure 3. (a) SEM and SEM-EDS mapping images of O K, Co K, and Ni K, (b) TEM image, and (c) SAED pattern of CoNi/rGO-5/5. Inset of (c) showing the indices for the obtained SAED pattern.
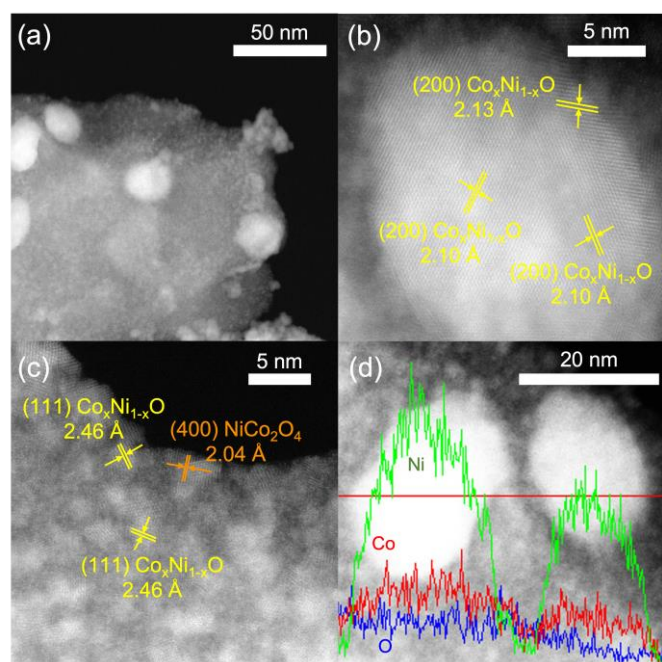

Figure 4. STEM-HAADF images of CoNi/rGO-5/5 catalyst. (b) STEM- HAADF image of a large nanoparticle at the top-left corner of (a), (c) STEM image of small nanoparticles, and (d) EDS elemental line profile of O K (blue), Co K (red), and Ni K (green) along the red line cross through two big nanoparticles in the HAADF image. Indices, measured d-spacing, and assignment for $Co_xNi_{1-x}O$ and for $NiCo_2O_4$ are written in yellow and brown in (b) and (c).

STEM-HAADF was employed to investigate the fine structure of the sample. Based on the contrast in **Figure 4a**, large nanoparticles around 15 nm and uniformly distributed, small nanoparticles of 2-3 nm on rGO were observed. The large nanoparticles in the STEM-HAADF image are consistent with that in TEM images. The small nanoparticles, which were not resolved clearly in the normal TEM due to their low-density contrast, were clearly visible in STEM-HAADF image. The large nanoparticles (**Figure 4b**) displayed a clear spacing of 2.10 Å, which corresponded to the (200) plane of $Co_xNi_{1-x}O$. Lattice spacings of small nanoparticles (**Figure 4c**) were measured to be 2.04 Å and 2.49 Å, corresponding to the (400) plane of $NiCo_2O_4$ and (111) plane of $Co_xNi_{1-x}O$ bimetallic oxides, respectively. This agrees with the results of XRD patterns and SAED patterns in the existence of both $NiCo_2O_4$ and $Co_xNi_{1-x}O$. Figure 4d displayed the

EDS elemental line profiles of the large nanoparticles in CoNi/rGO-5/5. The content of Ni was higher than Co in the $Co_xNi_{1-x}O$ large nanoparticles, that is, on average Co:Ni = 5:10 (mol/mol).

As shown in **Table 3**, in the large nanoparticles (10-20 nm) of all other catalysts with different Co:Ni feeding ratios, Ni content was always higher than Co and Co:Ni molar ratio was lower than the feeding molar ratio. Furthermore, the Co:Ni ratios of large $Co_xNi_{1-x}O$ nanoparticles measured using STEM-EDS (**Table 3**) were also lower than that estimated for $Co_xNi_{1-x}O$ using the XRD peak position (**Table 2**). This means that small $Co_xNi_{1-x}O$ nanoparticles contain more Co. The molar ratios of Co:Ni in small nanoparticles measured by STEM-EDS for all catalysts (**Table 3**) confirmed that small nanoparticles contained more Co than the feeding ratio. Among binary CoNi/rGO-i/j catalysts, CoNi/rGO-2/8 has both big and small nanoparticles with Ni-rich oxides. Other catalysts of CoNi/rGO-4/6, 5/5, 6/4, and 8/2 contain Ni-rich (molar ratio, Co:Ni = 0.5-0.7) in big $Co_xNi_{1-x}O$ nanoparticles and Co-rich (molar ratio, Co:Ni = 1.6-5.4) in small nanoparticles of $Co_xNi_{1-x}O$ and spinel $NiCo_2O_4$.

In summary, Co-rich non-stoichiometric spinel $NiCo_2O_4$ oxide was the main phase in CoNi/rGO-8/2 catalyst whereas $Co_xNi_{1-x}O$ bimetallic oxide and spinel $NiCo_2O_4$ were the main and minor phase, respectively, in CoNi/rGO-6/4, 5/5, 4/6, and 2/8 catalysts. The $Co_xNi_{1-x}O$ bimetallic oxides with large particle size (10-20 nm) were Ni-rich nanoparticles (Co:Ni (mol/mol) $\leqslant$ 0.5). The $Co_xNi_{1-x}O$ bimetallic oxides with small particle size (2-3 nm) were Co-rich nanoparticles (Co:Ni (mol/mol) $\geqslant$ 1.6) in CoNi/rGO-6/4, 5/5, and 4/6 catalysts. Meanwhile, spinel $NiCo_2O_4$ was also formed in small nanoparticles (2-3 nm). The mol% of spinel (as stoichiometric spinel) were of 2-13 % and decreased with the increase of Ni in the order of Co:Ni = 6/4 (13%), 5/5 (12%), 4/6 (4%), and 2/8 (2%). Ni-rich oxides presented in both small and big $Co_xNi_{1-x}O$ bimetallic oxides nanoparticles and small spinel nanoparticles of CoNi/rGO-2/8.

The formation of large sized Ni-rich $Co_xNi_{1-x}O$ nanoparticles and small sized Co-rich nanoparticles of $Co_xNi_{1-x}O$ and spinel $NiCo_2O_4$ was studied by analyzing the thermal decomposition of $Co(NO_3)_2 \cdot 6H_2O/GO$, $Ni(NO_3)_2 \cdot 6H_2O/GO$, and equimolar Co-Ni nitrate/GO by TG-DTA. It is found that $Co(NO_3)_2$ started to decompose at around 145 °C to form Co_3O_4 and ~ 250 °C to form CoO whereas $Ni(NO_3)_2$ started to decompose at 235 °C to form NiO (Figure S6).[41, 42] When both metal nitrates existed in the synthesis of catalysts, upon heating $Co(NO_3)_2$ could form Co_3O_4 first, which nucleated on the GO and/or rGO sheets with more anchoring sites and grew to form small oxide nanoparticles. As the temperature increased, $Ni(NO_3)_2$ decomposed. Part of Ni^{2+} replaced Co^{2+} in Co_3O_4 and became $NiCo_2O_4$ small particles because of lower crystal field stabilization energy. The other Ni^{2+} anchored on the GO sheets with less unoccupied anchoring sites at high temperature and formed large NiO nanoparticles (200-250 °C). Loss of oxygen functional groups on GO sheets with temperature further increasing led to the reduction and decomposition of $NiCo_2O_4$.

ARTICLE   Journal Name

Table 3. STEM-EDS compositions of nanoparticles in CoNi/rGO-i/j catalysts

|	Sample CoNi/rGO-i/j	8/2	6/4	5/5	4/6	2/8
Co:Ni (mol/mol)	Feeding ratio	8:2 (= 4)	6:4 (= 1.5)	5:5 (= 1)	4:6 (= 0.7)	2:8 (= 0.25)
	Big nanoparticles (9-18 nm)	8:12.04 (= 0.7)	6:13.18 (= 0.5)	5:10.40 (= 0.5)	4:8.64 (= 0.5)	2:10.45 (= 0.2)
	Small nanoparticles (2-3 nm)	8:1.49 (= 5.4)	6:3.45 (= 1.7)	5:2.65 (= 1.9)	4:2.54 (= 1.6)	2:7.82 (= 0.3)
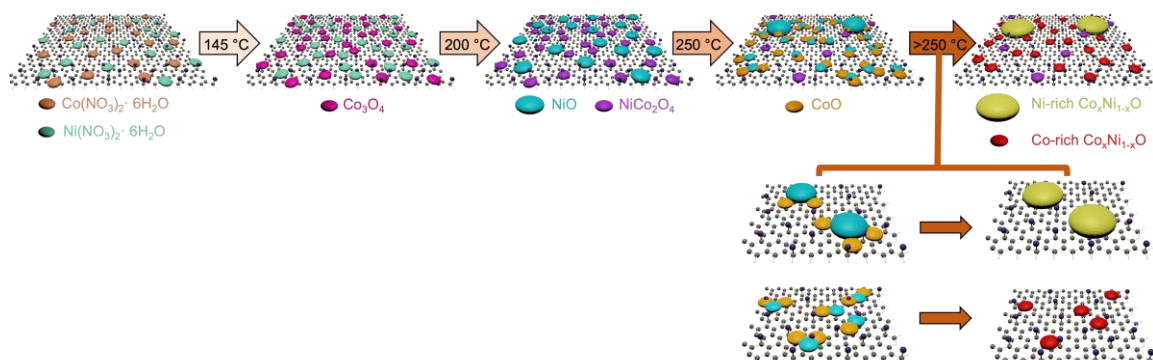
Figure 5. Formation of large sized Ni-rich $Co_xNi_{1-x}O$ nanoparticles and small sized Co-rich $Co_xNi_{1-x}O$ and $NiCo_2O_4$ nanoparticles.

$Co_xNi_{1-x}O$ derived from $NiCo_2O_4$ has small particle size with higher Co amount because of higher amount of Co in $NiCo_2O_4$. And the other decomposed CoO joined NiO large particles and formed $Co_xNi_{1-x}O$ large particles with Ni-rich. However, there was still $NiCo_2O_4$ remaining because the temperature was not high enough for the reduction of the metal oxides (>400 °C). The formation mechanism is illustrated in **Figure 5**.

3.2. Electrochemical Test Results

3.2.1. ORR Catalytic Activity of CoNi/rGO Catalysts CV test was conducted to investigate the catalytic activity in Ar- and O_2-saturated 1 M KOH electrolyte with a stationary RDE. **Figure 6a** is CV for CoNi/rGO-5/5 catalyst and **Figure S7** contains CV results of catalysts with other Co:Ni molar ratios. A typical oxygen reduction peak in the CV curve of the CoNi/rGO-5/5 catalyst was detected at ~1 mA·cm^{-2} with the onset potential, $E_{onset-CV}$, at 0.72 V (**Figure 6a**). The ORR onset potential of CoNi/rGO-5/5 was slightly higher than that of catalysts (**Table 4**) of other Co:Ni molar ratios (0.68-0.70 V). The ORR onset potentials of all samples were lower than that of Pt/C reference catalyst (0.86 V, **Figure S8**).

ORR activity was further evaluated by LSV in O_2-saturated 1 M KOH electrolyte at different rotation speeds of the RDE. **Figures 6b**, **S7**, **S8** and **S9** plotted the LSV results of CoNi/rGO-5/5, catalyst of other Co:Ni molar ratios, commercial Pt/C reference ORR catalyst and CoNiMix/rGO, respectively, at 1600 rpm. CoNiMix/rGO was obtained by physically mixing CoNi/rGO-10/0 and CoNi/rGO-0/10 1:1 (wt/wt). The results including onset potential, $E_{onset-LSV1600rpm}$ at -0.2 mA·cm^{-2}, and halfway potential, $E_{1/2-LSV1600rpm}$, were summarized in **Table 4**.
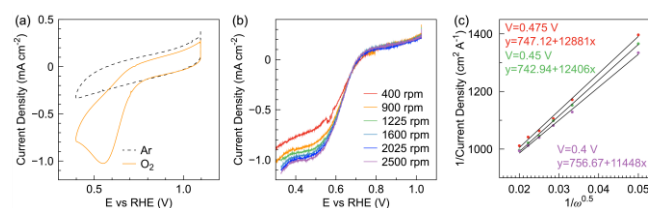
Figure 6. Electrochemical test results of CoNi/rGO-5/5: (a) CV curves in Ar-saturated electrolyte (black, dashed curve) and in O_2-saturated electrolyte (yellow, solid curve), (b) LSV curves at rotation speeds from 400 to 2500 rpm, and (c) K-L plots.

CoNi/rGO-5/5 and CoNiMix/rGO both had the highest $E_{onset-LSV1600rpm}$ (0.66 V) and $E_{1/2-LSV1600rpm}$ (0.63 V) among CoNi/rGO catalysts with different metal ratios. However, $E_{onset-LSV1600rpm}$ and $E_{1/2-LSV1600rpm}$ of CoNi/rGO-i/j catalysts were of 0.62-0.66 V and 0.61-0.63 V, respectively, without significant difference among them. They were lower compared with the Pt/C reference catalyst ($E_{onset-LSV1600rpm}$ = 0.87 V, $E_{1/2-LSV1600rpm}$ = 0.81 V). Thus, at low current density (<1 mA·cm^{-2}), there was no obvious difference in ORR performance in terms of onset and halfway potentials among catalysts of different Co:Ni molar ratios.

Furthermore, LSV with different rotation speeds from 400 to 2500 rpm was conducted to evaluate the electron-transfer reaction mechanism in ORR of the CoNi/rGO-i/j catalysts and Pt/C reference (**Figures 6b, S7, S8** and **S9**). Koutecky-Levich (K-L) plots for CoNi/rGO-5/5 catalyst revealed a linear relationship between diffusion limited current density with the rotation speed, implying ORR is a kinetic-controlled process. According to the K-L plots, the electron-transfer numbers, n, were of 3.44 ~ 3.87 (average: n = 3.63), which is slightly lower than that of the Pt/C of 3.68 ~ 3.87 (average: n = 3.77). Thus, a nearly four-electron reaction pathway can be considered for CoNi/rGO-5/5,

exhibiting a good ORR performance.[43-45] On the other hand, CoNiMix/rGO and other catalysts displayed lower electron-transfer numbers (average: n = 2.45-3.26), suggesting a mixed 2- and 4- electron reaction pathway (**Table 4**). CoNi/rGO-0/10 (only NiO) and Ni-rich catalyst, CoNi/rGO-2/8, performed worse (n = 2.45-2.46), which was followed by CoNi/rGO-10/0 (only CoO, n = 2.74), whereas other CoNi/rGO-8/2 to 4/6 had better electron transfer numbers (n ~ 2.77-3.63). For CoNiMix/rGO (mixture of NiO and CoO single metal oxides on rGO sheets), though it achieved the same E_{onset} and $E_{1/2-1600rpm}$ with CoNi/rGO-5/5, the electron transfer number was much lower (2.65-2.89). This suggests the synergetic effect of the formation of binary oxide nanoparticles in enhancing the electron-transfer number comparing to the single metal catalysts and physical mixture of these two single metal oxides. Moreover, Ni-rich catalyst, CoNi/rGO-2/8, contained both big and small nanoparticles with Ni-rich oxides whereas other CoNi/rGO-8/2 to 4/6 contained Ni-rich $Co_xNi_{1-x}O$ big nanoparticles and small Co-rich nanoparticles of $Co_xNi_{1-x}O$ and spinel (**Table 3**). Results of ORR performance and structure-composition characteristics revealed that the NiO and Ni-rich oxides delivered lower ORR electron-transfer number than CoO and Co-rich oxides. Furthermore, since big nanoparticles are Ni-rich $Co_xNi_{1-x}O$ bimetallic oxides (**Table 3**), we can expect that the small nanoparticles of Co-rich oxides in CoNi/rGO-8/2 to 4/6 are responsible for the enhanced catalytic ORR performance in CoNi/rGO via affording high electron-transfer number. CoNi/rGO-8/2 catalyst was composed of non-stoichiometric spinel whereas CoNi/rGO-6/4 to 4/6 composed of both $Co_xNi_{1-x}O$ bimetallic oxides and spinel $NiCo_2O_4$ (13-4 mol%) wherein spinel mol % decreases with increasing Ni ratio. Judging from the crystal structure/composition and ORR electrochemical performance of the catalyst, it can be considered that both small Co-rich $Co_xNi_{1-x}O$ bimetallic oxides and spinel are active in ORR. However, since the best ORR performance belonged to CoNi/rGO-5/5 of only 12 mol% of spinel, we suspected that the Co-rich $Co_xNi_{1-x}O$ bimetallic oxides are more important in ORR performance of CoNi/rGO-i/j (50 wt% loading) compared with spinel $NiCo_2O_4$. The highest ORR performance may be related to the highest Co:Ni in bimetallic oxides in small nanoparticles (nearly 2:1 (mol/mol)) and large amount of spinel $NiCo_2O_4$ in CoNi/rGO-5/5.

When varying the metal loadings, CV and LSV tests for evaluating the ORR catalytic activity (**Figure S10**) showed similar $E_{onset-CV}$, $E_{onset-LSV1600rpm}$, and $E_{1/2-LSV1600rpm}$ for metal loadings ratios of 20-80 wt% (**Table 4**). The values are similar to that of CoNi/rGO-5/5. It is worth noting that only rGO also had good $E_{onset-CV}$ due to the contribution of non-Faradaic current from adsorption of O_2 to its high surface area for ORR. The high surface area of rGO was consistent with the largest electrochemical surface area observed in CV scan in Ar-saturated electrolyte of rGO compared with other CoNi/rGO catalysts (**Figure S10**). The electron-transfer numbers of catalyst with 50 and 60 wt% metal loadings were of 3.63 and 3.50, respectively, suggesting ORR with a close 4-electron transfer pathway. They are higher than that with 40 and 80 wt% metal loadings, that is, 2.73 and 2.45, respectively, wherein ORR with

mixed 2- and 4-electron transfer pathway was likely to have occurred. These results indicate that in catalysts containing rGO, medium metal loadings of 50-60 wt% allow the highest electron transfer wherein too low or too high metal loadings reduce that number. This can be caused by weak ORR activity of rGO when it is abundant ($\leq$ 40 wt%) and severe aggregation of catalyst at high metal loading (80 wt%). In contrast, CoNi/rGO-100 wt% (no rGO, only metal oxides) displayed a highest $E_{onset-CV}$ (0.85 V), $E_{onset-LSV1600rpm}$ (0.7 V), $E_{1/2-LSV1600rpm}$ (0.64 V), and electron-transfer number (3.85) (**Table 4**). The $E_{onset-CV}$ and electron-transfer number values were similar to that of the reference Pt/C (**Table 4**). While the reason for this is not clear, it is possibly due to the existence of a significant amount of stoichiometric spinel $NiCo_2O_4$ with high ORR performance in the sample.

3.2.2. OER Catalytic Activity of CoNi/rGO Catalysts OER catalytic activity is an important property in evaluating bifunctional catalytic performance when applying the catalyst in rechargeable ZAB (**Figure 7**).

Table 4. Summary of electrochemical test results of catalysts with different Co:Ni molar ratios (CoNi/rGO-i/j), metal loadings (CoNi/rGO-w wt%), Pt/C reference catalysts and CoNiMix/rGO.

Samples	$E_{onset-CV}$ (V)	$E_{onset-LSV1600rpm}$ (V)	$E_{1/2-LSV1600rpm}$ (V)	Electron transfer number			
				0.400 V	0.450 V	0.475 V	Average
CoNi/rGO-i/j							
10/0	0.69	0.64	0.61	2.89	2.65	2.67	2.74
8/2	0.70	0.64	0.62	3.15	2.85	2.84	2.95
6/4	0.70	0.62	0.61	2.72	2.84	2.75	2.77
5/5	0.72	0.66	0.63	3.87	3.57	3.44	3.63
4/6	0.69	0.63	0.61	3.19	3.38	3.20	3.26
2/8	0.68	0.63	0.62	2.45	2.54	2.38	2.46
0/10	0.70	0.64	0.61	2.54	2.39	2.43	2.45
Ref: Pt/C	0.86	0.87	0.81	3.87	3.76	3.68	3.77
CoNiMix/rGO	0.71	0.66	0.63	2.89	2.65	2.67	2.74
CoNi/rGO-w wt%							
0 wt%	0.8	0.77	0.69	NA	NA	NA	NA
20 wt%	0.77	0.68	0.66	NA	NA	NA	NA
40 wt%	0.71	0.65	0.63	2.89	2.65	2.67	2.73
50 wt%	0.72	0.66	0.63	3.87	3.57	3.44	3.63
60 wt%	0.69	0.65	0.63	3.61	3.63	3.26	3.50
80 wt%	0.69	0.65	0.62	2.64	2.33	2.39	2.45
100 wt%	0.85	0.70	0.64	3.98	3.83	3.74	3.85

LSV were collected for CoNi/rGO catalysts of 3 representative Co:Ni ratios, that is, 10/0 (only CoO), 5/5 ($Co_xNi_{1-x}O$ bimetallic oxide and spinel $NiCo_2O_4$), and 0/10 (mainly NiO). The results showed increasing OER onset potential in the order of CoNi/rGO-10/0, CoNi/rGO-5/5, and CoNi/rGO-0/10. This indicates that in OER activity, CoO is better than NiO and there is no synergistic effect by making Ni and Co oxides in bimetallic or spinel structures for current densities of 0-22 mA·cm^{-2}. This is different from the obvious synergetic effect of CoNi bimetallic oxides in ORR. This suggests that there is an optimal ratio of Co and Ni when CoNi/rGO is used as bifunctional ORR/ORR catalyst.

However, though it was just the mixture of CoNi/rGO-10/0 and 0/10, CoNiMix/rGO displayed a lower OER catalytic activity than both single metal catalysts, which indicated the OER catalytic property of binary metal oxides.
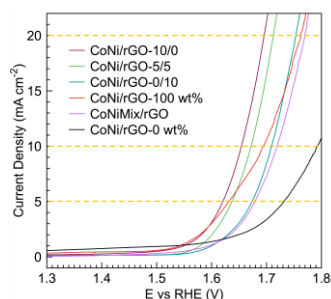

Figure 7. LSV curves of CoNi/rGO-10/0, 5/5, 0/10, 100 wt%, CoNiMix/rGO and rGO measured in 1 M KOH at 1600 rpm for the study of OER activities of the catalysts.

In terms of OER performance, the CoNi/rGO-10/0 and 5/5 displayed a low OER potentials of 1.654 and 1.672 V, respectively, at the current density of 10 mA·cm⁻², which were comparable to that of Ir/C (1.61 V) and Ru/C (1.62 V) as traditional noble metal catalysts (**Table 5**).[46]

Furthermore, only rGO (metal loading of 0 wt%) showed severe corrosion in OER with the highest OER onset potential among all tested samples. This clearly shows that the OER catalytic effect comes from metal oxides. Moreover, we expected that rGO is not able to maintain cycle stability in rechargeable ZABs when it is used as bifunctional catalyst. In terms of the impact of the metal loading on OER performance, it is interesting to note that at a very low current densities (< 5 mA·cm⁻²), CoNi/rGO-100 wt% (only metal oxides) displayed the lowest potential compared with CoNi/rGO-0 wt% (only rGO) and CoNi/rGO-50 wt%. However, as the current density increased, the OER potential of CoNi/rGO-100 wt% increased way faster than the other catalysts with both metal oxides and rGO (e.g., CoNi/rGO-50 wt%, CoNi/rGO-10/0). Over 20 mA·cm⁻², CoNi/rGO-100 wt% displayed the highest OER potential (lowest OER catalytic activity) among CoNi/rGO samples. This indicated that the bimetallic oxides catalyst without rGO would have a poor OER performance at high current density (100 mA·cm⁻²) used in our ZAB battery test. Thus, we can expect that this catalyst with the best ORR performance (highest $E_{onset-CV}$, $E_{onset-LSV1600rpm}$, and n) may still deliver bad cycle performance in ZABs at high current density for their poor OER activity (highest OER $E_{onset-LSV1600rpm}$).

The catalysts were further evaluated for bifunctional ORR/OER catalytic activity by taking the voltage difference (ΔE) between the OER potential at current density of 10 mA·cm⁻² (E_{OER10}) and the half-wave potential of ORR ($E_{1/2-LSV1600rpm}$).[32,47] For electrochemical devices, current density is of practical importance, for which the smaller the difference between the ORR and OER potentials, the better does the catalyst perform in bifunctional ORR/OER application.[46,48,49] The ΔE of the catalysts were listed in **Table 5**. The bifunctional character of CoNi/rGO-5/5 was the best among the catalysts with the smallest ΔE of 1.042 V (**Table 5**).

Table 5. Comparison of bifunctional ORR/OER activities among catalysts

Samples	$E_{OER0.5}$ (V)[a]	E_{OERS} (V)[a]	E_{OER10} (V)[a]	E_{OER20} (V)[a]	ΔE (V)[b]
CoNi/rGO-10/0	1.499	1.621	1.654	1.696	1.044
CoNi/rGO-5/5 (CoNi/rGO-50 wt%)	1.558	1.637	1.672	1.713	1.042
CoNiMix/rGO[c]	1.548	1.679	1.719	1.770	1.059
CoNi/rGO-0/10	1.575	1.674	1.709	1.753	1.099
CoNi/rGO-100 wt% (only CoNi oxides)	1.471	1.631	1.694	1.762	1.054
CoNi/rGO-0wt% (only rGO)	1.240	1.732	1.792	1.886	1.102
20 wt% Ir/C[46]			1.61		
20 wt% Ru/C[46]			1.62		

[a]$E_{OER0.5}$, E_{OERS}, E_{OER10}, and E_{OER20} were measured at 0.5, 5, 10, and 20 mA·cm⁻², respectively, in LSV anodic scan (OER) at 1600 rpm in Ar-saturated electrolyte; [b]ΔV = V_{OER10} - $V_{1/2-LSV1600rpm}$.

At such a low current density, the synergetic effect of two metal oxides does not manifest in terms of bifunctional characteristics. CoNi/rGO-0 wt% (only rGO) possessed a higher initial OER current density, in which case the $E_{OER0.5}$ was lower than the others. However, as the current density increased, the potential became larger than that of CoNi/rGO catalysts, causing poor bifunctional performance. CoNi/rGO-100 wt% possessed the smallest difference between ORR and OER resulting from the high ORR catalytic activity. However, as mentioned above, the current densities driven from ORR and OER test with CV and LSV are much lower than our target of 100 mA·cm⁻², and for CoNi/rGO-100 wt% OER activity becomes the worst at higher current densities. Thus, it is necessary to examine this sample in ZAB to have a solid conclusion of its actual performance at high current density.

3.3. Battery Performance

CoNi/rGO catalysts with different metal molar ratio and different metal loading amount were used as the ORR/OER catalysts in air cathode in lab-scale ZABs. The battery tests were carried out for comparative cycle stability, evaluated at a current density of 100 mA·cm⁻² with 1 h discharging and 1 h charging as one full cycle. 1 h discharging and charging was chosen based on preliminary analysis of the discharge profile (**Figure S11**). **Figure 8** shows voltage, current density, and discharge capacity of a battery using CoNi/rGO-5/5 catalyst for 40 cycles, which provided the best battery performance among all the catalysts. Current density of 100 mA·cm⁻² started to decrease after cycle 12, with a further decrease at cycle 31, and initial discharge current could not be maintained at 100 mA·cm⁻² after 31 cycles (**Figure 8b**). This reflected in the fading of discharge capacity (**Figure 8c**).
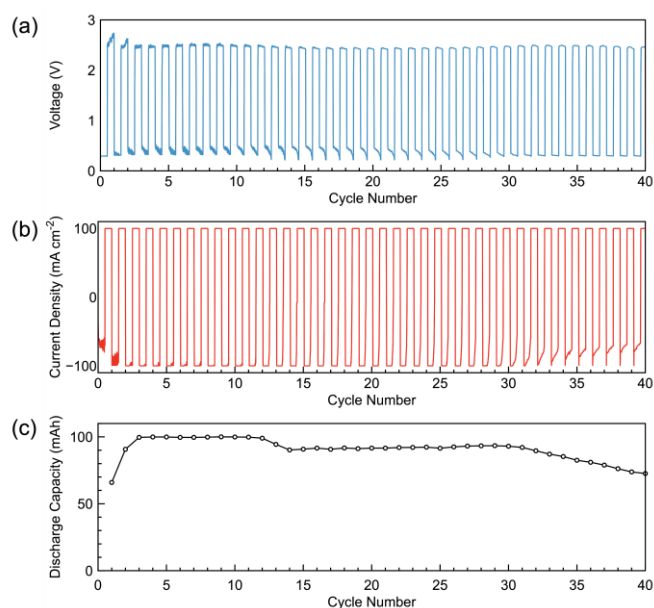
Figure 8. Discharge-charge cycle test results of a ZAB at 100 mA·cm^{-2} using CoNi/rGO-5/5 catalyst for air cathode: (a) voltage profile, (b) current density profile, and (c) discharge capacity over cycle.

Charging current density was maintained at 100 mA·cm^{-2} over all cycles (**Figure 8b**). Thus, the cycle stability was compared among the catalysts by counting the number of cycles with discharging capacity over 95 and 90 mAh (95 and 90%, respectively, of the maximum discharge capacity). For 31 continuous cycles (62 h), the battery using CoNi/rGO-5/5 catalyst maintained its activity with 90 mAh discharge capacity (**Figure 8c**). This implies excellent cycling stability under high current density.

The average cycle numbers of more than 95 and 90 mAh discharge capacity for samples with different metal molar ratio were plotted in **Figure 9a** and **9b**, respectively, in which each catalyst was applied to 8 cells in the cycling test. CoNi/rGO-10/0 and CoNi/rGO-0/10 displayed poor stability performance, implying the poor stability and catalytic activity of monometallic oxide catalysts. For both 95 and 90 mAh discharge capacity, ZABs using CoNi/rGO-10/0 catalysts delivered more cycle numbers than those using CoNi/rGO-0/10. ZABs using Co-rich catalyst, i.e., CoNi/rGO-8/2, performed much better than those using Ni-rich catalyst, i.e., CoNi/rGO-2/8. These results agree well with better ORR (i.e., electron-transfer number) and OER (*i.e.*, potential) activities of CoO compared with NiO and Ni-rich Co$_x$Ni$_{1-x}$O obtained in the previous section. As for the discharge capacity over 95 mAh (**Figure 9a**) of catalysts containing both Co and Ni, the cycle numbers for ZABs using CoNi/rGO-i/j from 8/2 to 4/6 showed no significant difference (13 to 16 cycles). Under the condition of discharge capacity over 90 mAh, CoNi/rGO-5/5 displayed the best cycle stability of 25 continuous cycles (~50 h). ZABs with CoNi/rGO-8/2 and 6/4 catalysts had slightly lower cycle numbers of 23. ZABs with CoNi/rGO-4/6 catalyst run for less than 20 cycles. Moreover, **Figure S12** shows the discharge and charge polarization curves at different current densities of ZAB with CoNi/rGO-10/0, 5/5, and 0/10. As observed, the discharge voltage loss with the increase of current density on

CoNi/rGO-5/5 was smaller than CoNi/rGO-10/0 and 0/10. The charge polarizations of ZAB using CoNi/rGO-5/5 and 10/0 also showed higher operating current density than that of CoNi/rGO-0/10. Thus, the results indicated the better recharge-ability for CoNi/rGO-5/5.[27] These results again confirmed that better cycle performance was associated with catalysts of Co-rich CoNi/rGO with pivotal role of small nanoparticles of Co-rich Co$_x$Ni$_{1-x}$O bimetallic oxides and spinel.
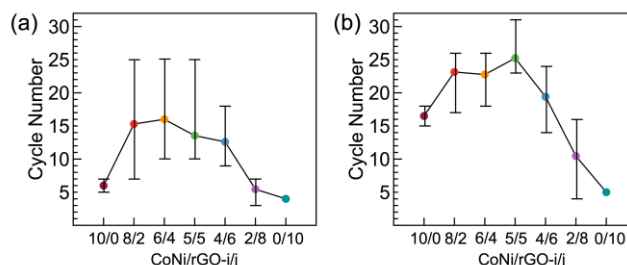

Figure 9. Average cycle numbers of samples with different Co:Ni ratios at 50% metal loading maintaining (a) 95% and (b) 90% discharge capacity. The error bars represent the minimum and the maximum number of cycles that ZABs using the catalysts performed in the cycle test. 8 ZABs were used in the cycle test for each catalyst.
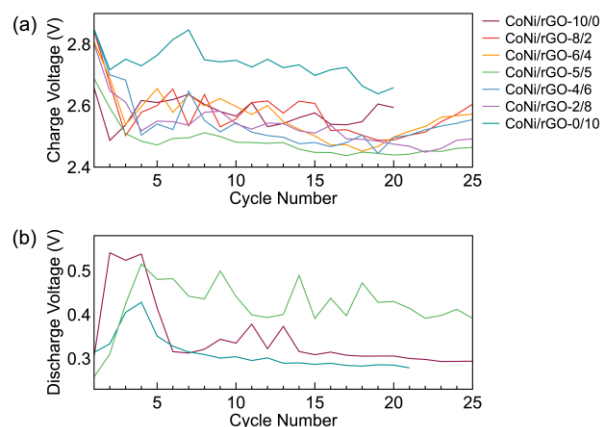

Figure 10. (a) Charge voltage at the end of each cycle using CoNi/rGO catalysts with different Co:Ni molar ratios, i.e., 10/0 (purple), 8/2 (red), 6/4 (orange), 5/5 (green), 4/6 (light blue), 2/8 (violet), and 0/10 (cyan), and (b) discharge voltage 5 min after the start of each cycle using catalysts CoNi/rGO-10/0 (purple), -5/5 (green) and -0/10 (cyan) in long-term cycle stability test of ZABs.

In electrochemical test with CV and LSV (at low current density), the synergetic effect of binary oxide catalysts compared with monometallic oxide catalysts were observed in ORR (*i.e.*, enhanced electron-transfer number in CoNi/rGO-5/5), but not in OER (OER potential increased in the order of CoNi/rGO-0/10 < CoNi/rGO-5/5 < CoNi/rGO-10/0), and ORR/OER bifunctionality. In contrast, at high current density, the synergetic effect by making binary oxide catalysts was also observed in the charge process where OER occurs. **Figure 10a** showed the charge voltage of ZABs using CoNi/rGO-i/j over cycles. CoNi/rGO-5/5 with lower charge voltage compared with CoNi/rGO-10/0 and 0/10 (monometallic oxides) suggests the synergetic effect of binary oxide catalyst at high current density operation. The lower the charge voltage, the less severe the carbon corrosion which causes catalyst removal (from the

electrode chemically and physically) and electrode decomposition. Consequently, more catalysts on stable cathodes can continue working in the discharge process. As for the discharge voltage displayed in **Figure 10b**, CoNi/rGO-5/5 showed the highest discharge voltage among the three samples, implying good ORR property and cycle stability under high current density. This agrees with the ORR electrochemical test results. Besides, the discharge voltage of each cycle of CoNi/rGO-5/5 remained at high voltage within 25 cycles, and the discharge voltage for each cycle at 1, 5, 10, and 30 min showed no big difference (**Figure S13**). This also indicates the high stability of CoNi/rGO-5/5 maintaining stable discharge voltage under high current density during each cycle. Thus, the ZABs can maintain its discharge/charge performance for longer run at high current density. Moreover, the discharge voltage of CoNi/rGO-10/0 and 0/10 decreased after 15 and 5 cycles separately, which was the cycle test result maintaining over 90% of maximum discharge capacity of each sample. This could be related to the carbon corrosion during the charging process which damaged the carbon materials in catalysts. In which case, the deactivated catalysts may cause the 2-electron ORR reaction pathway to be preferred during discharging, which led to the decrease in discharge potential.
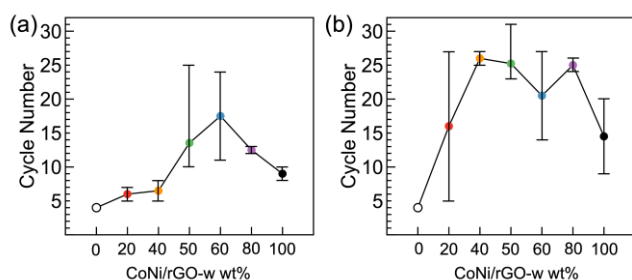

Figure 11. Average cycle numbers of ZABs using CoNi/rGO catalysts with different metal loadings maintaining (a) 95% and (b) 90% discharge capacity. The error bars represent the minimum and the maximum number of cycles of different ZAB cells using same catalysts.

Overall, the charge voltage of ZABs using CoNi/rGO-5/5 catalyst was the lowest among ZABs using different Co:Ni molar ratios. This suggests that at high current density, small Co-rich bimetallic oxides and spinel in CoNi/rGO-5/5 are not only the best in ORR performance but also good for OER activity. Furthermore, the highest charge voltage of ZABs using CoNi/rGO-0/10 (NiO) catalyst was consistent with their worst cycle stability.

Figure 11 shows the summary of the discharge-charge cycle test results of ZABs using catalysts with different metal loadings and same ratio of Co:Ni = 5:5 (mol/mol), in which each catalyst was applied to 2 cells in the cycling test. The details of cycle test results are in **Figure S14**. ZAB with rGO lasted only 4 cycles (8 h) for 95 and 90 % discharge capacity because of the low OER catalytic activity of the bare rGO, which caused severe electrode corrosion (C corrosion) in charge process and, thus, destroyed the electrode. The highest charge voltage of ZAB using rGO catalyst compared with other CoNi/rGO catalysts was observed (**Figure S15**). Similar issue was thought to cause the drop of

discharge capacity to below 95 % in few subsequent cycles of ZABs using catalysts 20 and 40 wt% loadings. Using only CoNi oxide catalyst without rGO (CoNi/rGO-100 wt%), ZAB displayed a longer average stability of 9 and 14.5 cycles over 95 and 90% discharge capacity, respectively, compared with that of ZAB using the bare rGO catalyst. This implies the catalytic property of the oxides in improving both the ORR and OER performance, particularly, the stoichiometric spinel $NiCo_2O_4$. This is because the bare oxide catalyst contained stoichiometric $NiCo_2O_4$ and NiO (Figure S3). However, as mentioned previously NiO is not good for both ORR and OER (**Tables 3 and 4**). Moreover, samples with both $Co_xNi_{1-x}O$ bimetallic oxides and $NiCo_2O_4$ embedded on rGO exhibited higher stability of over 16 cycles for 90%, which were more than CoNi/rGO-100 wt%. This indicates the role of Co-rich bimetallic oxides and spinel $NiCo_2O_4$ in lowering the OER potential and improving the ORR electron-transfer number examined at high current density. Thus, the ORR/OER bifunctionality which was not observed at low current density in electrochemical test, clearly presented in high current density cycle test of ZAB. The stability performance of ZABs using catalysts with loadings from CoNi/rGO-40 wt% to 80 wt% showed no significant difference in obtaining 90 % discharge capacity whereas catalysts without rGO or without CoNi oxides exhibited bad cycle stabilities. The role of rGO as the dispersion substrate prevented metal oxide nanoparticles from agglomerating and contributed to the stability of the oxide catalyst over cycles.

Conclusions

CoNi/rGO as bifunctional ORR/OER electrocatalysts have been successfully prepared by a simple thermal decomposition of metal nitrates in GO. The CoNi/rGO catalysts were found to be composed of $Co_xNi_{1-x}O$ bimetallic oxide and spinel $NiCo_2O_4$ nanoparticles uniformly dispersed on rGO. It was found that in CoNi/rGO-8/2, 6/4, 5/5, and 4/6 catalysts, Ni-rich bimetallic oxide formed large nanoparticles (10-20 nm) while Co-rich bimetallic oxide and spinel existed in small nanoparticles (2-3 nm). In CoNi/rGO-2/8, however, there were only Ni-rich nanoparticles. Electrochemical test revealed that the CoO and Co-rich bimetallic oxides were more active in both ORR and OER than NiO and Ni-rich oxides. Furthermore, small nanoparticles of Co-rich $Co_xNi_{1-x}O$ bimetallic oxide and spinel $NiCo_2O_4$ were active in ORR/OER. At low current densities in electrochemical tests (ORR: $\leq$ 1 mA·cm^{-2}, OER: < 20 mA·cm^{-2}), binary oxides exhibited synergetic effect in terms of improving ORR electron-transfer number whereas the synergetic effect was not observed in OER activity wherein OER performance decreased from CoNi/rGO-0/10 to CoNi/rGO-5/5 and CoNi/rGO-0/10. At high current density of 100 mA·cm^{-2} in ZAB test, synergistic effect of binary CoNi oxides and of co-existence of CoNi-oxide and rGO in CoNi/rGO-5/5 was also evidenced for lowering charge voltage (OER process), which resulted in the best ZAB cycle performance of 31 cycles (62h) maintaining more than 90% capacity. The results from varying the metal loadings on rGO revealed that $Co_xNi_{1-x}O$ and $NiCo_2O_4$ provided ORR/OER bifunctional catalytic activity while the rGO sheets was

ARTICLE   **Journal Name**

beneficial for electron transport and dispersion of catalysts for stable performance. Cycle stability was found to be limited by the charging process, in which C corrosion was an issue.

Author Contributions

The manuscript was written through contributions of all authors. All authors have given approval to the final version of the manuscript.

Conflicts of interest

There are no conflicts to declare.

Acknowledgements

Notes and references

1   https://sdgs.un.org/goals.
2   X. Yu and A. Manthiram, *Adv. Energy Sustainability Res.,* 2021, **2**, 2000102.
3   N. Radenahmad, R. Khezri, A. A. Mohamad, M. T. Nguyen, T. Yonezawa, A. Somwangthanaroj and S. Kheawhom, *J. Alloys Compd.,* 2021, **883**, 160935.
4   N. Borchers, S. Clark, B. Horstmann, K. Jayasayee, M. Juel and P. Stevens, *J. Power Sources,* 2021, **484**, 229309.
5   J. Pan, Y. Y. Xu, H. Yang, Z. Dong, H. Liu and B. Y. Xia, *Adv. Science,* 2018, **5**, 4, 1700691.
6   W. Kao-ian, M. T. Nguyen, T. Yonezawa, R. Pornprasertsuk, J. Qin, S. Siwamogsatham and S. Kheawhom, *Mater. Today Energy,* 2021, **21**, 100738.

7   M. Etesami, A. A. Mohamad, M. T. Nguyen, T. Yonezawa, R. Pornprasertsuk, A. Somwangthanaroj and S. Kheawhom, *J. Alloys Compd.,* 2021, **889**, 161738.
8   M. P. Clark, M. Xiong, K. Cadien and D. G. Ivey, *ACS Appl. Energy Mater.,* 2019, **3**, 603-613.
9   D. Yang, L. Zhang, X. Yan and X. Yao, *Small Methods,* 2017, **1**, 1700209.
10   Y. Li and H. Dai, *Chem. Soc. Rev.,* 2014, **43**, 5257-5275.
11   Z. Cui, G. Fu, Y. Li and J. B. Goodenough, *Angew. Chem. Int. Ed.,* 2017, **56**, 9901-9905.
12   J. Park, M. Park, G. Nam, M. G. Kim and J. Cho, *Nano Lett.,* 2017, **17**, 3974-3981.
13   E. Davari, A. D. Johnson, A. Mittal, M. Xiong and D. G. Ivey, *Electrochim. Acta,* 2016, **211**, 735-743.
14   M. G. Park, D. U. Lee, M. H. Seo, Z. P. Cano and Z. Chen, *Small,* 2016, **12**, 20, 2707-2714.
15   Z. Song, X. Han, Y. Deng, N. Zhao, W. Hu and C. Zhong, *ACS Appl. Mater. Interfaces,* 2017, **9**, 22694-22703.
16   D. Banham, S. Ye, K. Pei, J.-i. Ozaki, T. Kishimoto and Y. Imashiro, *J. Power Sources,* 2015, **285**, 334-348.
17   W. Gou, J. Bian, M. Zhang, Z. Xia, Y. Liu, Y. Yang, Q. Dong, J. Li and Y. Qu, *Carbon,* 2019, **155**, 545-552.
18   Y. Bu, O. Gwon, G. Nam, H. Jang, S. Kim, Q. Zhong, J. Cho and G. Kim, *ACS Nano,* 2017, **11**, 11594-11601.
19   L. Wei, H. E. Karahan, S. Zhai, H. Liu, X. Chen, Z. Zhou, Y. Lei, Z. Liu and Y. Chen, *Adv. Mater.,* 2017, **29**, 1701410.
20   D. Chen, C. Chen, Z. M. Baiyee, Z. Shao and F. Ciucci, *Chem. Rev.,* 2015, **115**, 9869-9921.
21   B. Cui, H. Lin, J.-B. Li, X. Li, J. Yang and J. Tao, *Adv. Funct. Mater.,* 2008, **18**, 1440-1447.
22   M. Prabu, K. Ketpang and S. Shanmugam, *Nanoscale,* 2014, **6**, 3173-3181.
23   Q. Huang, X. Zhong, Q. Zhang, X. Wu, M. Jiao, B. Chen, J. Sheng and G. Zhou, *J. Energy Chem.*, 2022, **68**, 679-687.
24   Y. Wang, R. Gan, H. Liu, M. Dirican, C. Wei, C. Ma, J. Shi and X. Zhang, *J. Mater. Chem. A*, 2021, **9**, 2764-2774.
25   X. He, Y. Tian, Z. Huang, L. Xu, J. Wu, J. Qian, J. Zhang and H. Li, *J. Mater. Chem. A*, 2021, **9**, 2301-2307.
26   G. Du, X. Liu, Y. Zong, T. S. Andy Hor, A. Yu and Z. Liu, *Nanoscale,* 2013, **5**, 4657-4661.
27   D. Bin, Z. Guo, A. G. Tamirat, Y. Ma, Y. Wang and Y. Xia, *Nanoscale,* 2017, **9**, 11148-11157.
28   C. Zhou, X. Chen, S. Liu, Y. Han, H. Meng, Q. Jiang, S. Zhao, F. Wei, J. Sun, T. Tan and R. Zhang, *J. Am. Chem. Soc.*, 2022, **144**, 2694-2704.
29   X. Hu, T. Yang, Z. Yang, Z. Li, R. Wang, M. Li, G. Huang, B. Jiang, C. Xu and F. Pan, *J. Mater. Sci. Technol.*, 2022, **115**, 19-28.
30   B. J. Park, H. Lee, J. Kim and H. S. Park, *J. Ind. Eng. Chem.*, 2022, **109**, 413-421.
31   K. Hung, S. Hosseini, T. Ko, C. Tseng and Y. Li, *Fuel*, 2022, **316**, 123328.
32   B. Gao, M. Tan, W. Xi, X. Lin, Z. Li, M. Shen and B. Lin, *J. Power Sources*, 2022, **527**, 231205.
33   J. Liu, Z. Luo, X. Zhang, H. Zheng, L. Peng, D. Qian, C. Jia, D. Sun-Waterhouse and G. I. N. Waterhouse, *J. Mater. Chem. A*, 2021, **9**, 27701-27708.
34   T. T. Nguyen, J. Balamurugan, K. Lau, N. H. Kim and J. H. Lee, *J. Mater. Chem. A*, 2021, **9**, 9092-9104.
35   W. J. Sim, M. T. Nguyen, Z. Huang, S. Kheawhom, C. Wattanakit and T. Yonezawa, *Nanoscale*, in press, DOI : 10.1039/D2NR01258H
36   P. T. Nam, N. Van Khanh, N. T. Thom, N. T. Phuong, N. Van Trang, N. T. Xuyen, V. Q. Thai, V. A. Tuan and D. T. Mai Thanh, *Vietnam J. Chem.,* 2018, **56**, 778-785.
37   C. Fu, G. Zhao, H. Zhang and S. Li, *Int. J. Electrochem. Sci.,* 2013, **8**, 6269 - 6280.
38   A. R. Denton and N. W. Ashcroft, *Phys. Rev. A,* 1991, **43**, 3161-3164.

39 L. Vegard and Z. Physik, *Z. Phys.,* 1921, **5**, 17-26.
40 T. Wang, Y. Li, H. Li, D. Shi, Q. Jiao, Y. Zhao, P. Su, W. Wang and Q. Wu, *ACS Omega,* 2020, **5**, 26253-26261.
41 W. Brockner, C. Ehrhardt and M. Gjikaj, *Thermochim. Acta,* 2007, **456**, 64-68.
42 B. Małecka, A. Łącz, E. Drożdż and A. Małecki, *J. Therm. Anal. Calorim.,* 2014, **119**, 1053-1061.
43 M. Gopalakrishnan, A. A. Mohamad, M. T. Nguyen, T. Yonezawa, J. Qin, P. Thamyongkit, A. Somwangthanaroj and S. Kheawhom, *Mater. Today Chem.,* 2022, **23**, 100632.
44 J. Li, Y. Wang, T. Zhou, H. Zhang, X. Sun, J. Tang, L. Zhang, A. M. Al-Enizi, Z. Yang and G. Zheng, *J. Am. Chem. Soc.,* 2015, **137**, 14305-14312.
45 H.-L. Jia, J. Zhao, L. Gu, Z.-J. Peng, Z.-L. Bao, X.-L. Sun and M.-Y Guan, *Sustain. Energy Fuels,* 2020, **4**, 6165-6173.
46 Y. Gorlin and T. F. Jaramillo, *J. Am. Chem. Soc.,* 2010, **132**, 13612-13614.
47 Y. Zheng, H. Song, S. Chen, X. Yu, J. Zhu, J. Xu, K. A. I. Zhang, C. Zhang and T. Liu, *Small*, 2020, **16**, 2004342.
48 D. Wang, X. Chen, D. G. Evans and W. Yang, *Nanoscale,* 2013, **5**, 5312-5315.
49 W. G. Hardin, D. A. Slanac, X. Wang, S. Dai, K. P. Johnston and K. J. Stevenson, *J. Phys. Chem. Lett.,* 2013, **4**, 1254-1259.